Precursory slow-slip loaded the 2009 L'Aquila earthquake sequence

A. Borghi,[1,2] A. Aoudia,[1] F. Javed[1,3] and R. Barzaghi[4]

[1]*International Centre for Theoretical Physics, Strada Costiera,* 11, *I-34151 Trieste, Italy. E-mail:* aoudia@ictp.it
[2]*Università degli Studi eCampus, Novedrate, Italy*
[3]*University of Trieste, Trieste, Italy*
[4]*Politecnico di Milano, Milano, Italy*

SUMMARY

Slow-slip events (SSEs) are common at subduction zone faults where large mega earthquakes occur. We report here that one of the best-recorded moderate size continental earthquake, the 2009 April 6 moment magnitude (M_w) 6.3 L'Aquila (Italy) earthquake, was preceded by a 5.9 M_w SSE that originated from the decollement beneath the reactivated normal faulting system. The SSE is identified from a rigorous analysis of continuous GPS stations and occurred on the 12 February and lasted for almost two weeks. It coincided with a burst in the foreshock activity with small repeating earthquakes migrating towards the main-shock hypocentre as well as with a change in the elastic properties of rocks in the fault region. The SSE has caused substantial stress loading at seismogenic depths where the magnitude 4.0 foreshock and M_w 6.3 main shock nucleated. This stress loading is also spatially correlated with the lateral extent of the aftershock sequence.

Key words: Satellite geodesy; Transient deformation; Creep and deformation.

1 INTRODUCTION

Predicting future earthquakes remains impossible even when they are preceded by foreshocks, as foreshocks generally cannot be distinguished from other small-earthquake sequences (e.g. Chen & Shearer 2013; Brodsky & Lay 2014). The recent L'Aquila, Central Italy, 2009 earthquake was assigned low chances of occurrence using prior foreshock observations (ICEF 2011). This is inherent to the understanding of the mechanisms that stand behind the foreshocks and the difficulty in their identification as such in due time. Data from recent subduction zone earthquakes, the 2011 M_w 9.0 Tohoku, Japan (Kato *et al.* 2012), and the 2014 M_w 8.1 Iquique, North Chile (Brodsky & Lay 2014), identified persistent nucleation of similar foreshock events migrating towards the future main-shock nucleation region that seem to be distinctive precursors for these two events. Specifically for the Tohoku earthquake the set of foreshocks that includes some repeating families of seismic events suggest the occurrence of a slow-slip event (SSE; Kato *et al.* 2012). In continental regions, the 1999 M_w 7.6 Izmit, Turkey, earthquake (Bouchon *et al.* 2011), exhibited a phase of slow-slip at the base of the brittle crust prior to some main shocks. Observations from Japan and Turkey, confirmed that these two types of different interplate earthquakes, subduction and transform, sometimes may exhibit slow-slip prior to the main shock. Such a behaviour may have probably taken place prior to a number of interplate earthquakes (Bouchon *et al.* 2013).

The moderate size M_w 6.3 April 6th L'Aquila earthquake was preceded by an important foreshock sequence clustered near the base of the activated fault plane and repeaters were identified in the vicinity of the nucleation region (Chiaraluce *et al.* 2011; Valoroso *et al.* 2013). Furthermore, the seismic wave propagation yielded important changes, in the fault region, of the elastic properties of rocks prior to the earthquake (Lucente *et al.* 2010).

In this context, we analysed continuous Global Positioning System (GPS) time-series, prior to the 2009 L'Aquila earthquake (Fig. 1a) in search of any transient deformation. We compare evidence for a SSE from GPS data with seismological constraints and characterize the stress loading on the eventual rupture plane.

2 THE 2009 L'AQUILA SEQUENCE

The M_w 6.3 L'Aquila earthquake (Fig. 1) caused 308 casualties and damaged a wide area. The seismic sequence (Fig. 1b) ruptured a NW-SE trending normal fault system in a region that has been interseismically extending NE-SW at a background rate of ~2 mm yr^{-1} (D'Agostino *et al.* 2011). The main shock nucleated at a depth of 8.27 km (Valoroso *et al.* 2013) and ruptured an 18 km long fault (Cirella *et al.* 2009). The aftershock sequence (Valoroso *et al.* 2013) and the afterslip distribution (Anzidei *et al.* 2009; Gualandi *et al.* 2014) clearly show a much larger reactivated area, reaching ~50 km of lateral extent. Aftershock data with more than 46.000 events (Chiaraluce *et al.* 2011; Valoroso *et al.* 2013) were relocated to provide an unprecedented resolution of the geometry of the faulting. These data provided a unique image of the geometry of the activated fault system, namely the L'Aquila
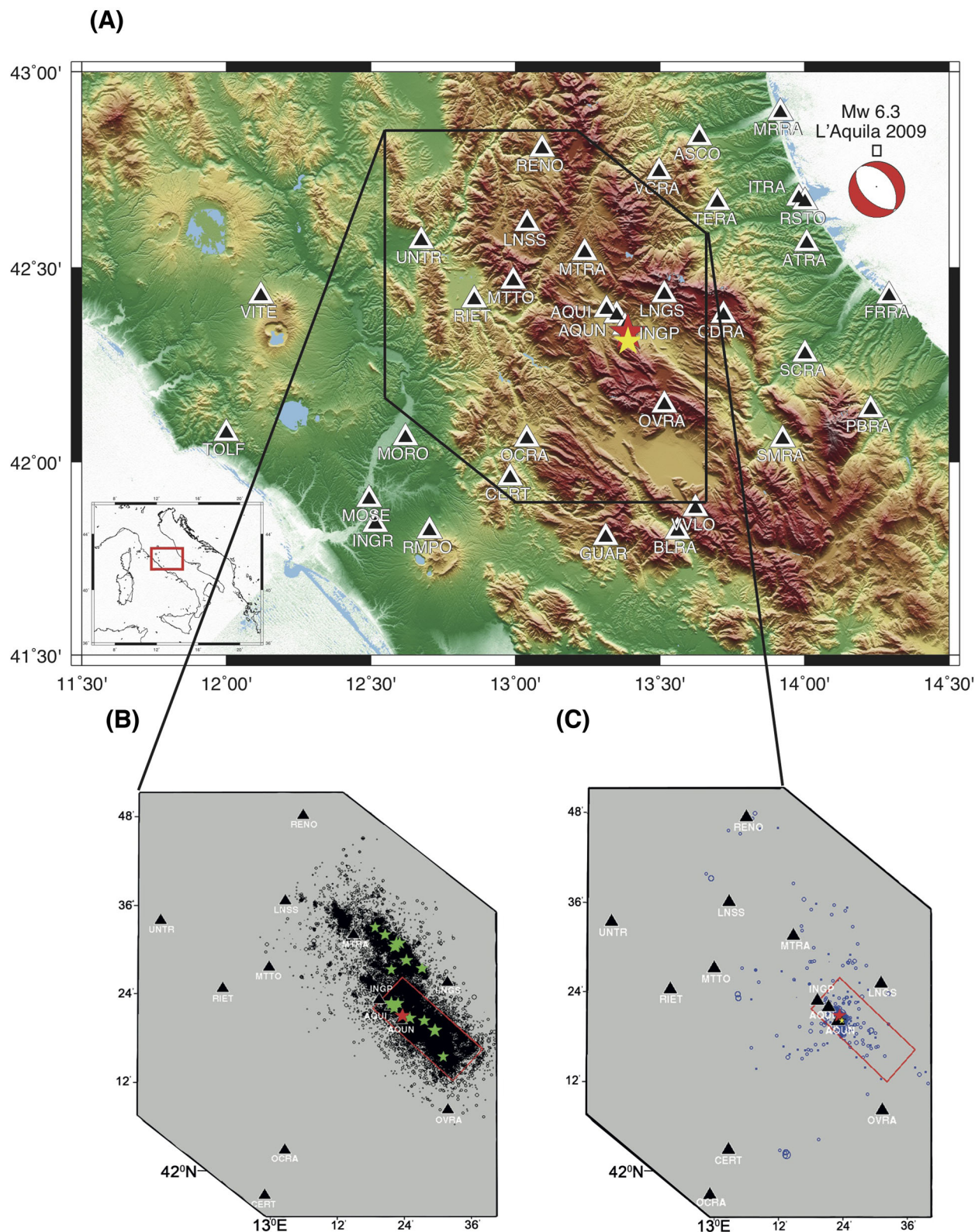
Figure 1. (A) The 2009 April 6 L'Aquila, Central Italy, earthquake (red star also in panels B and C; focal mechanism from Cirella *et al.* 2009) and March 30th magnitude 4 foreshock (yellow star also in panel C). (B,C) Zoom on the L'Aquila aftershock and foreshock sequence (Valoroso *et al.* 2013), green stars are aftershocks with magnitude equal or larger than 4, blue circles are foreshocks and the red rectangle represents the surface projection of the rupture area of the main shock (Cirella *et al.* 2009). Black triangles are Continuous GPS stations operating since 2007. The DEM used in the plot is derived by Shuttle Radar Topography Mission (SRTM-3)

fault to the south, the Campotosto fault to the north and associated antithetic faults. Additionally the study on the aftershock sequence increased the resolution on the foreshock distribution and allowed the identification of repeaters at the seismicity cut-off depth. At this depth a detachment has been clearly reported at the base of the high-angle normal faults and likely characterized by a creeping behaviour (Chiaraluce *et al.* 2011; Chiaraluce 2012; Valoroso *et al.* 2013). It is worth highlighting that the foreshocks extended far away from the main-shock fault rupture and over an area almost larger in size than the aftershock extent (Figs 1b and c). Furthermore, the temporal variations of seismic velocity and anisotropy revealed important changes in the elastic properties of the medium during the preparatory phase of the main shock (Lucente *et al.* 2010). Complementary to seismological data, GPS data sets were used to study both the coseismic (e.g. Anzidei *et al.* 2009) and postseismic deformation (D'Agostino *et al.* 2012; Gualandi *et al.* 2014).

3 GPS DATA ANALYSIS

We used GPS data (Devoti *et al.* 2011) to investigate transient deformation prior to the earthquake. We analysed time-series of 29 continuous GPS stations (Fig. 1a) that do not present sizeable data gaps within the 6 months prior to the main shock. The available data start from 2007.

The GPS time-series, that is the evolution in time of each co-ordinate component (north, east and up, in a topocentric system), can be fitted by a functional model $f(t_i; \mathbf{x})$, which describes the tectonic linear movement of the site, the amplitude of the periodic signals and the magnitude of the known discontinuities detected in the time-series coordinate (i.e. changes of instrument; Nikolaidis 2002). All these geophysical quantities are represented by the parameter vector $\mathbf{x}$, which has been estimated using a least-squares method. Concerning the frequencies of the periodic signals (annual and/or semi-annual), we determined their precise values by the analysis of the periodogram, instead of fixing the value to 1 cpy and 0.5 cpy to avoid the GPS draconitic effect (Ray *et al.* 2008). In the least-squares estimation of the functional parameters $\mathbf{x}$, a proper stochastic model has been used, accounting for the white and the time-correlated noise, which can be described by means of power-law noise (Agnew 1992) with fractional estimation of the power (Williams 2003; Williams 2008). Furthermore, the data have been reduced for the spatially correlated noise, the so-called common mode error (CME). This regional filtering has been performed estimating epoch by epoch a common bias for all stations (Wdowinski *et al.* 1997). This stacking approach seems to be a reasonable choice for this type of regional network.

Transients are defined as a different behaviour of the GPS time-series with respect to the steady state for a finite time interval. In most of the cases, they are not clear in the data because the signal is hidden by noise and not detectable by a simple eye investigation of the time-series (Supporting Information Fig. S1). To increase the signal-to-noise ratio filtering techniques are applied both in the spatial and temporal domains using different methods, like moving average, Kalman filter, Principal Component Analysis (PCA), etc. The procedure used in this work resembles the method based on smoothing in time domain and PCA in space domain (Ji & Herring 2013). However, in our approach the data are filtered in time by Least-square Collocation (Koch 1977; Borghi *et al.* 2009), instead of using a Kalman filter based on first-order Gauss-Markov process (Ji & Herring 2013) for the reasons that will be discussed in the following paragraphs.

3.1 Temporal filtering

We started the investigation for possible transient signals, analysing the time-series of the residuals, after the estimate of the parameter vector $\mathbf{x}$.

In general, time-series $y(t_i)$ can be represented by eq. (1), given by the sum of a functional part $f(t_i; \mathbf{x})$, that describes the observation vector $\mathbf{y}$ in terms of parameter vector $\mathbf{x}$, a time correlated noise $\mathbf{s}$ and white noise $\mathbf{n}$:

$$y(t_i) = f(t_i; x) + s(t_i) + n(t_i) = f(t_i; x) + \varepsilon(t_i). \tag{1}$$

This type of data can be filtered using the Least-squares Collocation method (Koch 1977; Moritz 1980) to separate the white noise $\mathbf{n}$ from the correlated noise $\mathbf{s}$, called also signal in the stationary random process theory, obtaining the filtered signal $\hat{s}$ (eq. 2), knowing the covariance matrices C_{ss} and C_{nn} of the coloured and white noise respectively:

$$\hat{s} = C_{ss}(C_{ss} + C_{nn})^{-1}\varepsilon = C_{ss}(C_{ss} + \sigma^2 I)^{-1}\varepsilon. \tag{2}$$

In all of the sites of the processed network, the residual time-series $\boldsymbol{\varepsilon}$ satisfy the second-order stationarity behaviour in terms of mean and variance, that is, the mean $E[\boldsymbol{\varepsilon}(t)] = m$ and the second-order moment $E[\boldsymbol{\varepsilon}^2(t)] = m_2$ are constants and independent of t. Hence, the variance $\text{var}\{\boldsymbol{\varepsilon}(t)\}$ is also a constant and the covariance $\text{cov}\{\varepsilon(t_i), \varepsilon(t_j)\}$ is only dependent on the difference $(t_i - t_j)$, where t_i and t_j represent two different epochs. In this context, the autocovariance function (ACF) gives a complete knowledge of the stochastic properties of the data up to order 2, and the empirical ACF can be estimated, without any *a priori* assumption for the power spectrum of the signal. In eq. (3) is reported an 'unbiased' estimator of the sample ACF $C_{\varepsilon\varepsilon}$ of the signal $\varepsilon(t)$ for the time-lag τ (Priestley 1981).

$$\hat{C}_{\varepsilon\varepsilon}(\tau) = \frac{1}{N} \sum_{t=1}^{N-\tau} \varepsilon_t \varepsilon_{t+\tau}. \tag{3}$$

When the stationary condition is satisfied, the so-called stochastic approach of the least-squares collocation can be applied based on equation (2). In this equation, the auto-covariance matrices are computed using the positive defined model for the covariance function of the signal that better fit the empirical covariance values given by eq. (3). Thus, collocation is an adaptive filter because the filtering follows the stochastic structure of the data, using the empirical covariance function and its model, without any other *a priori* assumption, that is, the correlation length or power spectrum of the data. So, this type of filter increases the signal-to-noise ratio but preserves the high frequencies in the data. We believe that this aspect is important because the pattern of a possible transient is unknown and we would like to avoid strong smoothing of the data.

The least-squares collocation can be used both to filter and predict values to fill small data gaps. In Supporting Information Figs S2–S5, the time filtering of the residual time-series of some stations (MTTO, OCRA, AQUI, CERT) for the planimetric components are shown.

3.2 Spatial filtering

The research of transient signals assumes the hypothesis they are spatially correlated and will appear at multiple sites, otherwise the chance of detecting local phenomena is too high. The PCA technique is a way of identifying patterns in data, and expressing the data in such a way as to highlight their similarities and differences.
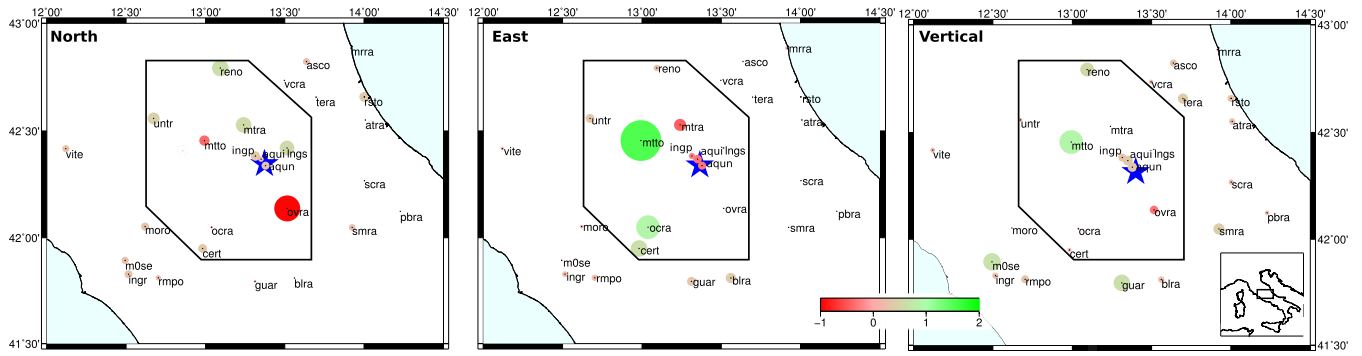
Figure 2. Contribution of each GPS station to the first principal component (PC), for the north, east and vertical component. The black polygon encloses the defined near-field stations. The blue star is the main shock. The colour bar and the size of the circles represent the magnitude of the eigenvectors.

Table 1. First four eigenvalues of the east, north and Up components of the coordinates for the three network designs: all stations available, only the closest stations to the L'Aquila main shock and the only distant stations (complementary to the near field). Values are in per cent.

	All stations (29)			Near field (11)			Far field (18)		
	E	N	U	E	N	U	E	N	U
PC$_1$	40.0	21.0	27.0	56.7	28.6	34.8	36.6	34.2	31.2
PC$_2$	17.3	17.3	12.3	14.0	24.3	21.4	17.4	21.4	18.2
PC$_3$	10.6	15.0	10.9	9.2	13.5	16.5	11.3	11.7	12.0
PC$_4$	7.5	9.9	9.8	6.5	11.5	11.2	7.3	7.8	8.7

PCA is often used in GPS network analysis to find out common features between stations that can be interpreted as spatially correlated errors, defined either as CME (Wdowinski *et al*. 1997) or geophysical signals like co-seismic deformation (Dong *et al*. 2006; Gualandi *et al*. 2014), ground water changes (Ji & Herring 2013) and seasonal signals (Tiampo *et al*. 2004). According to the definition of Jolliffe (2004), the central idea of this multivariate analysis method is to reduce the dimensionality of the data set consisting of a large number of variables, preserving as much the relevant information. This is performed by means of an orthogonal linear transformation to new set of uncorrelated variables, called principal components (PCs). The first PCs derived variables contain most of the information present in all of the original ones (Jolliffe 2004). Once the patterns have been found, the data can also be reconstructed by reducing the number of dimensions, without much loss of information, so this technique is also used for image compression.

At first the PCA analysis has been performed taking into account all the available 29 GPS stations (Fig. 1a). From the contribution of each station to PC1, we can assert that there is a group of 11 spatially correlated stations (Fig. 2) clustered around the hanging-wall of the reactivated fault zone. These stations present a higher value of the first eigenvalue, clearly distinct from the other PCs (Table 1 and Supporting Information Fig. S6). We call these 11 stations the near-field GPS stations. So, we restrict our analysis to the near-field stations, obtaining a better definition of PC1 especially for the east component, with a value of 56.7 per cent (Table 1). The MTTO site seems responsible for the highest contribution in the first PC, especially for the east component. However, by not accounting for this station, the power of the PC1 of the east component decreases slightly from 56.7 per cent (Table 1) to 46.4 per cent. So the MTTO site is considered as a crucial station rather than an outlier. In light of these considerations, we decide to continue the analysis using the solution based on the 11 near-field stations, and check this hypothesis.

We also compute the PCA using only the GPS stations far from the L'Aquila earthquake, defined far-field GPS stations, and finding a common pattern, especially for the planimetric coordinates, is difficult. It is worth highlighting that PC1 for the vertical component (Fig. 3) presents a well-determined weak common signal (about 30 per cent of variance, Table 1), independently of the solution used (near- or far-field), even if the signal-to-noise ratio is low which is inherent to the GPS vertical coordinate. So the method seems to resolve weak signals that suggests in our specific case that no transient affected the vertical component. PC1 amplitudes of the north component, for both near- and far-field stations (Fig. 3) differ, but no specific anomaly seems to appear. However the time evolution of PC1 for the east component exhibits a clear transient at epoch around 2009.1 when the near-field solution starts to diverge from the far-field solution (Fig. 3). The east component is the leading component of active extension across the Apennines (D'Agostino *et al*. 2011; D'Agostino 2014).

As reported by other investigators (i.e. Ji & Herring 2013) this sort of first PC tells us that a discontinuity has been recorded by most of the stations. In our case, we see the step function as an anomalous time-dependent discontinuity within the time-series, which is interpreted as an SSE.

We used a more formal statistical method in depicting transients in times series by applying a Bayesian procedure (de Lacy *et al*. 2008; Borghi *et al*. 2009) for each epoch of the first PCs (east, north, UP). The detection of the transients is based on the fitting of the data with a first order polynomial regression model that introduces a jump at an unknown epoch t. The discontinuity epoch t is detected by computing the marginal posterior distribution of the parameter t and then selecting the epoch with the highest *a posteriori* probability. The procedure has been applied to the time evolution of the first PC of east and north components. In the first case, the results show that at epoch 2009.1190 (12 February 2009) a transient of -3.93 ± 0.17 mm is detected with a maximum *a posteriori* probability (MAP) of 77.9 per cent (Fig. 3b). The *a posterior* distribution is centred from February 11 to February 13 with a total probability of a transient of 99.8 per cent. The transient vanishes around the 26 February (Fig. 3b). The transient clearly
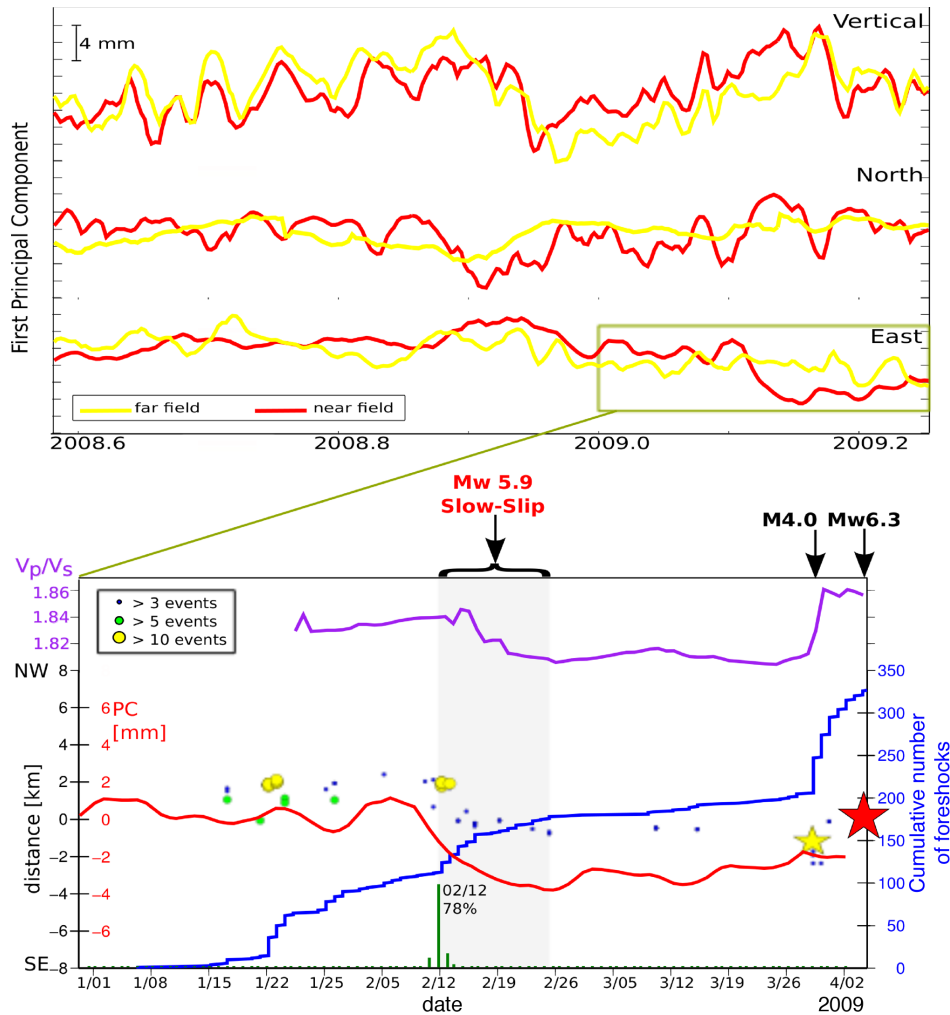
Figure 3. (a) Temporal evolution of the first principal component (PC) for the near-field and far-field GPS stations (stations inside and outside the polygon in Fig. 1a, respectively). (b) Zoom on the east first PC (red line), from January till April 9 2009; in purple the Vp/Vs ratio (Lucente *et al.* 2010); in blue the cumulative number of foreshocks whereas the blue, green and yellow dots are the numbers of repeaters (Valoroso *et al.* 2013); in green the histogram of the a posteriori probability distribution of the Bayesian discontinuities, with a MAP of about 78 per cent on February 12 at the start of the transient period related to the SSE shown in grey; yellow and red stars are foreshock and main shock, respectively. The *y*-axis with the label 'distance' represents the vertical plane along N133°E direction, where the foreshock events are projected. The origin of this *y*-axis is the L'Aquila main shock.

identified on the east component is less easily detectable on the northern component, where the Bayesian procedure is not able to point out any epoch with a significant probability.

4 GPS RESULTS VERSUS SEISMOLOGY

We next compared the geodetic transient with independent seismological observations (Lucente *et al.* 2010; Valoroso *et al.* 2013; Sugan *et al.* 2014) of the foreshock sequence available from 2009 January 1 until the main shock occurrence on 2009 April 6 (Fig. 3b). The transient mimics fairly well an important and sharp change in the Vp/Vs ratio. Lucente *et al.* (2010) focused on implications for fluid flow to explain the changes in Vp/Vs and anisotropy they found between the earlier and later foreshock periods. A clear anomaly is depicted between a magnitude 4.0 foreshock and the L'Aquila main shock a week later. However a second anomaly is clearly visible in the earlier foreshock period (Sugan *et al.* 2014) and it coincides fairly well with the timing of the geodetic transient. It is worth highlighting that the volume for which the study by Lucente *et al.* (2010) determined time variable Vp/Vs in the foreshock period com-

pares fairly well with the size of the lateral extent of the near-field GPS network we used in this study.

The start of the transient, 12th February, coincides with a new burst of seismic activity that tails off around the 26th of February when the transient vanishes. The repeaters started migrating and clustering around the nucleation region of the L'Aquila earthquake during the transient. It is worth highlighting that the large number of repeaters occurring right at the start of the transient decrease drastically during the transient with a complete shutdown at the end of the transient. These observations suggest that the geodetic transient recognised as a common signal from 11 near-field GPS stations corresponds to a SSE.

5 SSE AND STRESS LOADING

To extract the common transient from near-field stations, the reconstructed time-series including only the first PC, have been used. For each component a least-squares estimation of the discontinuity associated with the 12th February event has been computed and the values are reported in Table 2 and Fig. 4. The resulting displacement
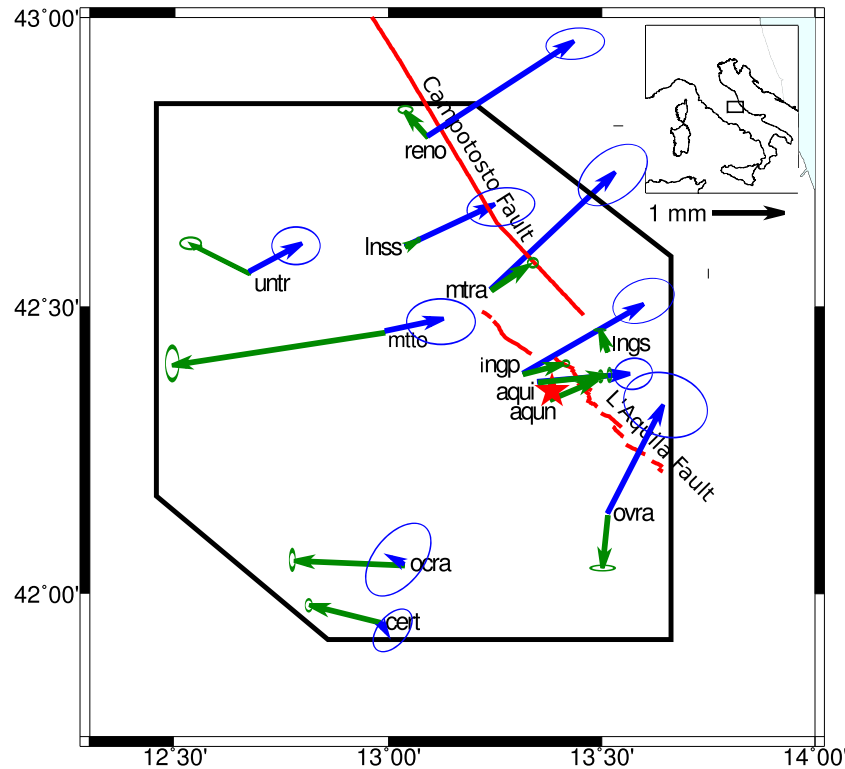
Figure 4. The blue vectors are yearly average interseismic displacement as recently computed by D'Agostino (2014); the green vector represent the displacement field computed over 2-week time from slow-slip event identified on the near-field GPS stations. The black polygon encloses the near-field GPS stations as in Fig. 2.

Table 2. Slow-slip event detected by the PCA analysis around epoch 2009 February 12. Values in (mm).

	North	East
AQUI	0.06 ± 0.01	0.96 ± 0.05
AQUN	0.19 ± 0.03	0.66 ± 0.03
CERT	0.21 ± 0.03	-1.00 ± 0.05
INGP	0.15 ± 0.02	0.57 ± 0.03
LNGS	0.42 ± 0.06	-0.11 ± 0.01
MTRA	0.38 ± 0.06	0.74 ± 0.04
MTTO	-0.37 ± 0.06	-2.97 ± 0.15
OCRA	0.05 ± 0.01	-1.56 ± 0.08
OVRA	-0.81 ± 0.12	-0.07 ± 0.01
RENO	0.28 ± 0.04	-0.33 ± 0.02
UNTR	0.39 ± 0.06	-0.74 ± 0.04

field is coherent with the tectonics of the region with a maximum extension along the eastern and northern components of almost 4 and 2.6 mm respectively over 14 d in a region with less than ~2 mm yr^{-1} of background rate (D'Agostino *et al*. 2011; D'Agostino 2014). Stations like MTTO, OVRA, UNTR and CERT situated at a distance of at least two times the locking depth from the L'Aquila fault zone, reverse their motion temporarily during the transient before resuming the usual long term motion (Fig. 4).

We next tested a range of possible fault slip models that best explains the observations. For doing so we followed a formal inversion of the derived GPS displacements (see Supporting Information) and provide a metric for assessing the relative fit of models (Okada 1985; Harris & Segall 1987; Jonsson *et al*. 2002). We then used the solutions reported in the Supporting Information (Appendix A: Figs 5c and d) as starting models for a trial and error forward model in order to improve the misfit values without adding complexity to the fault

model. Further to the dislocation surface that consists of a decollement we added antithetic faults as illustrated by the high-resolution aftershock and foreshock relocation (Chiaraluce 2012; Valoroso *et al*. 2013). The presence of the decollement is further confirmed by the flat nodal planes of the focal solutions as well as the existence of sparse seismicity beneath the decollement itself (Chiaraluce 2012). The slip model (Fig. 5) that best fits the GPS, with a misfit of 0.26 mm when compared with the computed vectors, consists then of a decollement with four patches very similar to the models represented in the Supporting Information (Appendix A: Figs 5c and d). The decollement located at 9.25 km, strikes parallel to the L'Aquila and Campostosto faults and dips 0.5 degree to the southwest. To fit the near fault GPS data we added two shallow antithetic faults and their geometry is defined by the aftershock distribution. The largest slip patch on the decollement reaches about 2 cm over an area of 160 km^2 right beneath L'Aquila fault. Approximately 2860 km^2 area slipped along the decollement during the SSE with an average slip of 0.9 cm. Adding to this the slip on the antithetic faults, the estimated total moment release by the SSE is equivalent to an $M_w \sim 5.9$ event. The major contribution to the total moment release comes from the slip on the decollement beneath the L'Aquila fault. We interpret motion on the antithetic faults as shallow and local accommodation of the deeper slip on the decollement.

We next used Coulomb 3.3.0.1 (Lin & Stein 2004; Toda *et al*. 2005) to resolve stress changes (Fig. 6) on the L'Aquila and Campotosto faults imposed by the 2009 February 12 M_w 5.9 SSE. We compute the Coulomb failure stresses with a friction coefficient of 0.4 and resolve stress changes on L'Aquila fault that increased with 1.1 bar at the hypocentre of the main shock (8.27 km) and over 2 bars at the hypocentre of the M4.0 March 30th foreshock (9.05 km). It is worth highlighting the striking correlation between the
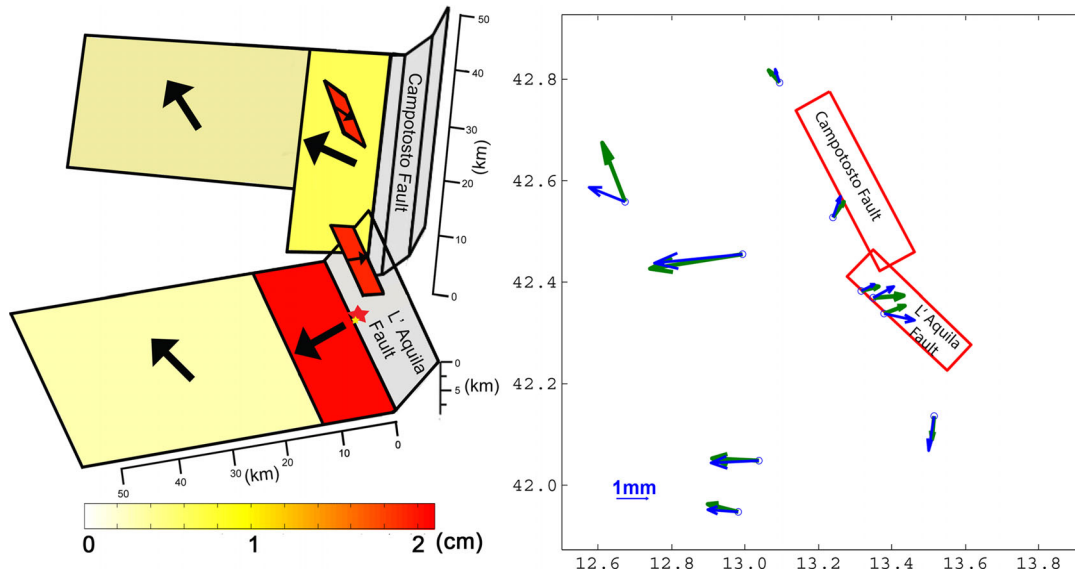
Figure 5. Forward model of the slip distribution on the decollement and antithetic faults (supplementary slip-model.txt online version) related to the SSE and the geometry of the reactivated fault system (Valoroso *et al*. 2013), yellow and red stars are March 30 foreshock and main shock, respectively. The map shows the fit between the observed (green) and the computed (blue) GPS from the slip model.
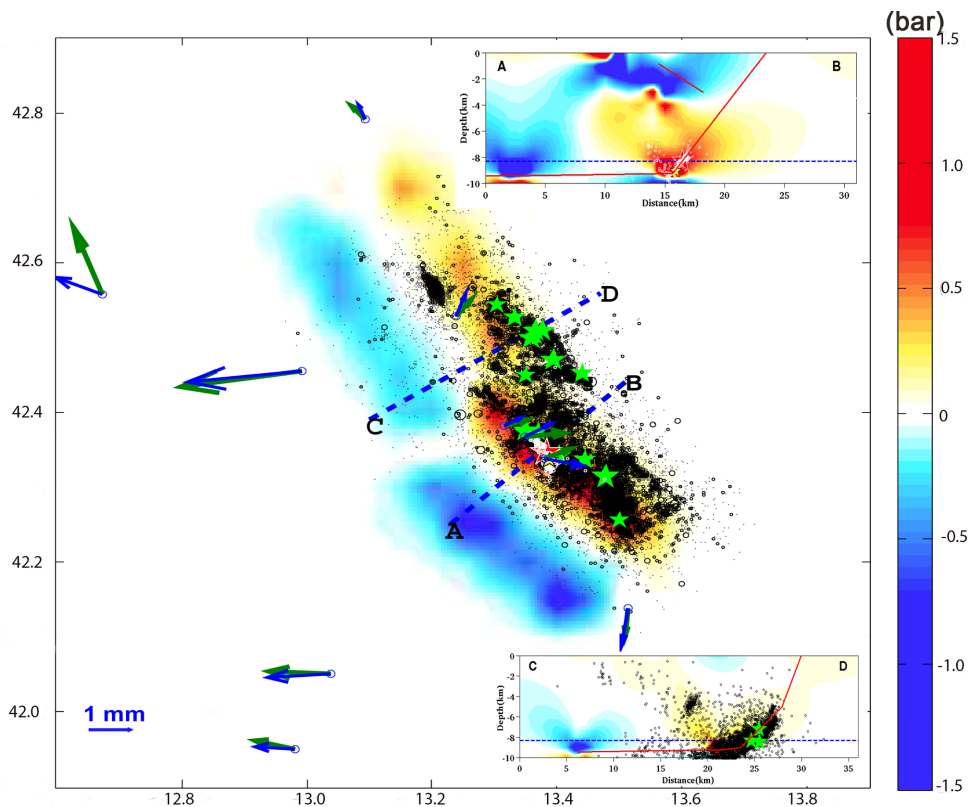

Figure 6. SSE Coulomb stress change and the L'Aquila main shock (in red), post February 12 foreshocks (white and the yellow star for March 30 magnitude 4) and aftershock sequence (green stars are aftershocks with magnitude equal or larger than 4). AB and CD are vertical sections across the reactivated L'Aquila and Campotosto faults, respectively. The green arrows are SSE observed GPS displacements while the blue arrows are computed using the slip model in Fig. 5.

positive stress change and the foreshock that took place after the 12th February and specifically those located on the deeper antithetic fault (Section AB, Fig. 6). Regarding the Campotosto fault (Section CD, Fig. 6) the increased stress change mimics fairly well the distribution of the aftershocks both on the fault and on the reactivated antithetic fault.

6 DISCUSSION AND CONCLUSION

It is conceivable that the SSE caused substantial stress loading on the hypocentre of the L'Aquila earthquake. The stress loading caused first the rupture of the M_w 4.0 foreshock, weakening therefore part of the geometrical barrier between the decollement and the

high-angle L'Aquila fault. The M_w 4.0 foreshock was then followed by a sequence of events, at the seismogenic depth, and mostly located on an antithetic fault accommodating the deformation on the geometrical barrier and favouring therefore fluid diffusion processes (Lucente *et al*. 2010) that contributed to the initiation of unstable dynamic rupture a week later.

We find that slip on the decollement increased the static stress at seismogenic depths. The spatial correlations between the Coulomb stress increase and the distribution of the unusual aftershock sequence are compelling. This suggests that the SSE loaded not only the M4.0 foreshock and M_w 6.3 main shock fault but also controlled the lateral distribution of the aftershocks that could not be otherwise explained by the stress change imposed by the L'Aquila main event.

It is clear for the L'Aquila case that no complete understanding of the foreshock sequence could have been achieved using the seismological data set only. Denser and integrated geodetic and seismological instrumentations are needed to depict slow-slip events in continental regions and understand their contribution to earthquake generation processes.

ACKNOWLEDGEMENTS

REFERENCES

Agnew, D., 1992. The time domain behaviour of power law noises, *Geophys. Res. Lett.,* **19,** 333–336.

Anzidei, M. *et al.*, 2009. Coseismic deformation of the destructive April 6, 2009 L'Aquila earthquake (central Italy) from GPS data, *Geophys. Res. Lett.,* **36,** L17307, doi:10.1029/2009GL039145.

Borghi, A., Aoudia, A., Riva, R. & Barzaghi, R., 2009. GPS monitoring and earthquake prediction: a success story towards a useful integration, *Tectonophysics,* **465,** 177–189.

Bouchon, M., Karabulut, H., Aktar, M., Ozalaybey, S., Schmittbuhl, J. & Bouin, M.P., 2011. Extended nucleation of the 1999 M_w 7.6 Izmit earthquake, *Science,* **331,** 877–880.

Bouchon, M., Durand, V., Marsan, D., Karabulut, H. & Schmittbuhl, J., 2013. The long precursory phase of most large interplate earthquakes, *Nat. Geosci.,* **6,** 299–302.

Brodsky, E.E. & Lay, T., 2014. Recognizing foreshocks from the 1 April 2014 Chile Earthquake, *Science,* **344,** 700–702.

Chen, X. & Shearer, P.M., 2013. California foreshock sequences suggest aseismic triggering process, *Geophys. Res. Lett.,* **40,** 2602–2607.

Chiaraluce, L., 2012. Unravelling the complexity of Apenninic extensional fault systems: a review of the 2009 L'Aquila earthquake (Central Apennines, Italy), *J. Struct. Geol.,* **42,** 2–18.

Chiaraluce, L., Valoroso, L., Piccinini, D., Di Stefano, R. & De Gori, P., 2011. The anatomy of the 2009 L'Aquila normal fault system (central Italy) imaged by high resolution foreshock and aftershock locations, *J. geophys. Res.,* **116,** doi:10.1029/2011JB008352.

Cirella, A., Piatanesi, A., Cocco, M., Tinti, E., Scognamiglio, L., Michelini, A., Lomax, A. & Boschi, E., 2009. Rupture history of the 2009 L'Aquila (Italy) earthquake from non-linear joint inversion of strong motion and GPS data, *Geophys. Res. Lett.,* **36,** L19304, doi:10.1029/2009GL039795.

D'Agostino, N., 2014. Complete seismic release of tectonic strain and earthquake recurrence in the Apennines (Italy), *Geophys. Res. Lett.,* **41,** 1155–1162.

D'Agostino, N., Mantenuto, S., D'Anastasio, E., Giuliani, R., Mattone, M., Calcaterra, S., Gambino, P. & Bonci, L., 2011. Evidence for localized active extension in the central Apennines (Italy) from global positioning system observations, *Geology,* **39,** 291–294.

D'Agostino, N., Cheloni, D., Fornaro, G., Giuliani, R. & Reale, D., 2012. Space-time distribution of afterslip following the 2009 L'Aquila earthquake, *J. geophys. Res.,* **117,** B02402, doi:10.1029/2011JB008523.

de Lacy, M.C., Reguzzoni, M., Sansò, F. & Venuti, G., 2008. The Bayesian detection of discontinuities in a polynomial regression and its application to the cycle-slip problem, *J. Geod.,* **82,** 527–542.

Devoti, R., Esposito, A., Pietrantonio, G., Pisani, A.R. & Riguzzi, F., 2011. Evidence of large scale deformation patterns from GPS data in the Italian subduction boundary, *Earth planet. Sci. Lett.,* **311**(3), 230–241.

Dong, D., Fang, P., Bock, Y., Webb, F., Prawirodirdjo, P., Kedar, S. & Jamason, P., 2006. Spatiotemporal filtering using principal component analysis and Karhunen-Loeve expansion approaches for regional GPS network analysis, *J. geophys. Res.,* **111,** B03405, doi:10.1029/2005JB003806.

Gualandi, A., Serpelloni, E. & Belardinelli, M.E., 2014. Space–time evolution of crustal deformation related to the M_w 6.3, 2009 L'Aquila earthquake (central Italy) from principal component analysis inversion of GPS position time-series, *Geophys. J. Int.,* **197**(1), 174–191.

Harris, R. & Segall, P., 1987. Detection of a locked zone at depth on the Parkfield, California segment of the San Andreas fault, *J. geophys. Res.,* **92,** 7945–7962.

ICEF, Operational earthquake forecasting. State of knowledge and guidelines for utilization, 2011. *Ann. Geophys.,* **54**(4), doi:10.4401/ag-5350.

Ji, K.H. & Herring, T.A., 2013. A method for detecting transient signals in GPS position time-series: smoothing and principal component analysis, *Geophys. J. Int.* **193,** 171–186.

Jolliffe, I.T., 2004. *Principal Component Analysis,* 2nd edn, Springer.

Jonsson, S., Zebker, H., Segall, P. & Amelung, F., 2002. Fault slip distribution of the 1999 M_w 7.1 Hector Mine earthquake, California, estimated from satellite radar and GPS measurements, *Bull. seism. Soc. Am.,* **92,** 1377–1389.

Kato, A., Igarashi, T., Tsuruoka, H., Nakagawa, S. & Hirata, N., 2012. Propagation of slow slip leading up to the 2011 M_w 9.0 Tohoku-Oki Earthquake, *Science,* **335,** 705–708.

Koch, K.-R., 1977. Least squares adjustment and collocation, *Bull. Geod.,* **51**(2), 127–135.

Lin, J. & Stein, R.S., 2004. Stress triggering in thrust and subduction earthquakes and stress interaction between the southern San Andreas and nearby thrust and strike-slip faults, *J. geophys. Res.,* **109,** B02303, doi:10.1029/2003JB002607.

Lucente, F.P., De Gori, P., Margheriti, L., Piccinini, D., Di Bona, M., Chiarabba, C. & Agostinetti, N.P., 2010. Temporal variation of seismic velocity and anisotropy before the 2009 M_w 6.3 L'Aquila earthquake, Italy, *Geology,* **38,** 1015–1018.

Moritz, H., 1980. *Advanced Physical Geodesy,* Abacus Press, 500 pp.

Nikolaidis, R., 2002. Observation of geodetic and seismic deformation with the Global Positioning System, *PhD thesis,* Univ. of Calif., San Diego.

Okada, Y., 1985. Surface deformation due to shear and tensile faults in a half-space, *Bull. seism. Soc. Am.,* **75**(4), 1135–1154.

Priestley, M.B., 1981. *Spectral Analysis and Time Series,* Academic Press.

Ray, J., Altamimi, Z., Collilieux, X. & van Dam, T., 2008. Anomalous harmonics in the spectra of GPS position estimates, *GPS Solut.,* **12,** 55–64.

Sugan, M., Kato, A., Miyake, H., Nakagawa, S. & Vuan, V., 2014. The preparatory phase of the 2009 M_w 6.3 L'Aquila earthquake by improving the detection capability of low-magnitude foreshocks, *Geophys. Res. Lett.,* **41,** 6137–6144.

Tiampo, K.F., Rundle, J.B., Klein, W., Ben-Zion, Y. & McGinnis, S., 2004. Using eigenpattern analysis to constrain seasonal signals in southern California, *Pure appl. Geophys.,* **161,** 1991–2003.

Toda, S., Stein, R.S., Richards-Dinger, K. & Bozkurt, S., 2005. Forecasting the evolution of seismicity in southern California: animations built on earthquake stress transfer, *J. geophys. Res.,* **110,** B05S16, doi:10.1029/2004JB003415.

Valoroso, L., Chiaraluce, L., Piccinini, D., Di Stefano, R., Schaff, S. & Waldhauser, F., 2013. Radiography of a normal fault system by 64,000 high-precision earthquake locations: the 2009 L'Aquila (central Italy) case study, *J. geophys. Res.,* **118,** 1156–1176.

Wdowinski, S., Bock, Y., Zhang, J. & Fang, P., 1997. Southern California Permanent GPS geodetic array: spatial filtering of daily positions for estimating coseismic and postseismic displacements induced by the 1992 Landers earthquake, *J. geophys. Res.,* **102,** 18 057–18 070.

Wessel, P. & Smith, W., 1991. Free software helps map and display data, *EOS, Trans. Am. geophys. Un.,* **72,** 441–461.

Williams, S.D.P., 2003. The effect of coloured noise on the uncertainties of rates estimated from geodetic time series, *J. Geod.,* **76,** 483–494.

Williams, S.D.P., 2008. CATS: GPS coordinate time series analysis software, *GPS Solut.,* **12,** 147–153.

SUPPORTING INFORMATION

Additional Supporting Information may be found in the online version of this paper:

Supplementary-Appendix A.

Figure S1. Time-series of east component of the CGPS sites used in the PCA analysis of the near-field stations: the black dots represent the original residuals; the red points the filtered values (see Supplementary Material in the digital version).

Figure S2. Time-series of the MTTO site for the north and east components, filtered by least-squares collocation (red line). Note the jump in the east component at epoch ~2009.1 (see Supplementary Material in the digital version).

Figure S3. Time-series of the AQUI site for the north and east components, filtered by least-squares collocation (red line) (see Supplementary Material in the digital version).

Figure S4. Time-series of the CERT site for the north and east components, filtered by least-squares collocation (red line) (see Supplementary Material in the digital version).

Figure S5. Time-series of the OCRA site for the north and east components, filtered by least-squares collocation (red line) (see Supplementary Material in the digital version).

Figure S6. First principal component of the east coordinate (red line) with the standard deviation. The transient is well resolved compared to the noise.

(http://gji.oxfordjournals.org/lookup/suppl/doi:10.1093/gji/ggw046/-/DC1).

Please note: Oxford University Press is not responsible for the content or functionality of any supporting materials supplied by the authors. Any queries (other than missing material) should be directed to the corresponding author for the paper.